Catalysis Communications 175 (2023) 106617

Contents lists available at ScienceDirect

Catalysis Communications

journal homepage: www.elsevier.com/locate/catcom

Carbon nitride from urea: Mechanistic study on photocatalytic hydrogen peroxide production for methyl orange removal

Laura S. Gómez Velázquez [a], María L. Dell'Arciprete [a,*], Lorean Madriz [a,b,c], Mónica C. Gonzalez [a,*]

[a] Instituto de Investigaciones Fisicoquímicas Teóricas y Aplicadas (INIFTA), CCT-La Plata-CONICET, Universidad Nacional de La Plata, La Plata, Argentina
[b] Instituto Tecnológico de Chascomús (INTECH), CCT-La Plata-CONICET, Chascomús, Provincia de Buenos Aires, Argentina
[c] Escuela de Bio y Nanotecnologías, Universidad Nacional de San Martín (UNSAM), Chascomús, Provincia de Buenos Aires, Argentina

ARTICLE INFO

Keywords:
Carbon nitride
Azo dyes
Hydrogen peroxide
Visible light
Urea
Reactive species
Vibrio Fischeri

ABSTRACT

Herein, we investigated the photocatalytic removal of methyl orange (MO) under 350 nm irradiation with carbon nitride (CN) nanoparticles from urea. Participation of photogenerated charge carriers and secondary reactive species in MO degradation process was evaluated by scavenging and photoelectrochemical assays. The experiments suggest that $HO^{\bullet}$ radicals are not only formed from the reaction of water with photogenerated holes, but via a three consecutive one-electron reduction of O_2 involving the formation of H_2O_2. The photocatalytic MO degradation mechanism was proposed. The present results emphasize the importance of charge carriers' separation in the optimization of CN photocatalysis for technological uses.

1. Introduction

Advance oxidation processes, which involve the generation of strong and non-selective oxidizing species turns out to be a viable alternative for pollutants degradation under ambient conditions without the production of harmful products [1]. Solar light-activated semiconductor photocatalyst have attracted widespread attention due to their potential in environmental and energy applications. Since the first report by Wang et al. [2], polymeric carbon nitride formed by repeating tri-*s*-triazine (heptazine) units, have emerged as an interesting metal-free catalyst. Despite its adequate band gap, low inner toxicity, and easiness of obtention, carbon nitride-based materials show some disadvantages as rapid charge recombination, low electrical conductivity and minor surface areas which result in weak photocatalytic efficiencies [3].

Alternative synthesis methods of H_2O_2 using H_2O and O_2 as precursors have gained interest as cleaner and economically processes [4]. In that sense, heterogeneous visible light-photocatalysts stand out as environmental friendly and efficient choice. In recent years, metal-free polymeric carbon nitride were emerged as promising photocatalyst for water splitting selectively producing H_2O_2 under visible light irradiation though oxygen reduction [5–7]. An hybrid photocatalyst of pyromellitic diimide-doped carbon nitride(g-C_3N_4/PDI) and reduced graphene(rGO) were prepared by Kofuji [8]. Photoexcitation of g-C_3N_4/PDI moiety leads to conduction band electrons transfer to rGO, causing the selective production of H_2O_2 *via* two-electron reduction of O_2 on the rGO surface. Grafting cationic polyethylenimine (PEI) molecules onto CN tune its electronic structure *via* intermolecular charge transfer, which improves the separation of photogenerated charge carriers [9]. Moreover, PEI promotes the two-electron O_2 reduction to H_2O_2 through a sequential two-step single-electron transfer route. Other authors proposed the formation of 1,4-endoperoxides as precursors for H_2O_2 synthesis. Shiraishi *et al* photoexcited g-C_3N_4 with visible light and observed the selective two-electron reduction of O_2 due to the efficient formation of 1,4-endoperoxide species on its surface which suppresses one-electron reduction of O_2 [10]. Furthermore, theoretical and experimental work performed by Wei and colleagues demonstrated that oxygen-enriched carbon nitride polymers can more easily form 1,4-endoperoxide species rather than superoxide radicals improving the efficiency of H_2O_2 production [11]. On the other hand, H_2O_2 combination with CN demonstrated excellent capability for photocatalytic degradation of methylene blue [12] and methyl viologen [13]. The solely presence of CN, without H_2O_2, is not enough to degrade these chromophores. According to the authors, the role of H_2O_2 in the photocatalytic process is to prevent recombination of charge carriers and to produce additional hydroxyl radicals. Hence, boosting the H_2O_2 production from CN may have industrial and environmental implications.

* Corresponding authors.
E-mail address: mlaura@inifta.unlp.edu.ar (M.L. Dell'Arciprete).

https://doi.org/10.1016/j.catcom.2023.106617
Received 23 November 2022; Received in revised form 14 January 2023; Accepted 24 January 2023
Available online 25 January 2023

Textile industries are one of major global polluters and consume high amounts of fuels and chemicals. The presence of textile dyes in water bodies significantly compromise their visual quality, increase biochemical and chemical oxygen demand, damage natural photosynthesis, inhibit plant growth and enter the food chain. Their accumulation in environmental compartments, including living organisms, may promote toxicity, mutagenicity and carcinogenicity [14]. Among them, azo dyes account for 70% of all the commercial dyes used in textile industries worldwide [15].

Although, discoloration of coloured water is an important parameter, the rupture of the dye chromophores might not improve the quality of the polluted water, as metabolites might show even greater toxicity than their precursors. [16] Therefore, identification of degradation products and evaluation of their toxicity are needed to stablish the oxidation stage of the dye required to observe a reduced toxicity.

Although, the synthesis and characterization of CN nanomaterials obtained from urea and their performance as photocatalyzers are well-reported in the literature, a detailed understanding of the photocatalytic azo dyes degradation mechanism and the role of photogenerated charge carriers and secondary reactive species, is still not fully understood. Herein, we obtained carbon nitride nanoparticles from the thermal treatment of urea and evaluated its photocatalytic mechanisms. As a probe, the reaction efficiency of methyl orange (MO) removal was determined in the presence of specific scavengers to assess the participation of the different reactive species in the degradation process, with particular interest in H_2O_2 generation and reaction. *Vibrio fischeri* bioluminescence assays allow the evaluation of the toxicity of MO and its degradation products. The identification of photocatalytic reaction products by LC-MS together with the above results allows the elucidation of the reaction mechanism.

2. Experimental section

2.1. Materials

Urea (ACS, Cicarelli), Methyl Orange (MO, Analar), Isopropyl alcohol (IPA, HPLC, Sintorgan), Ascorbic acid (AA, 99%, Carlo Erba), sodium azide (SA, 99%, Biopack,), hydrogen peroxide (H_2O_2, 30%, AR, Anedra) were used as received. Triethylamine (TEA, puriss p.a.), Methyl viologen dichloride hydrate (MV^{2+}, 98%) and catalase from bovine liver (lyophilized powder, 2000–5000 units/mg protein) were provided by Sigma-Aldrich. Aqueous solutions were prepared in ultrapure water (0.055 μS cm^{-1}) obtained from an OSMOION™ purification system.

2.2. Carbon nitride synthesis

The synthesis was performed by a thermal condensation method. Briefly, 5 g of urea dissolved in 2.5 mL of ultrapure water, the reaction mixture was placed in an alumina crucible and heated at 550 °C for 3 h (0.5 °C/ min). Later, the pale-yellow powder was washed with ultrapure water and dried in air at 80 °C for 8 h. The obtained nanoparticles were designed as CN.

2.3. Equipment

Electron microscopy images of the CN were acquired in a JEOL JEM-ARM200F equipment and alternatively in a FEI Talos 1162 microscope. The microscope was used in scanning TEM mode (STEM). A water suspension of CN was deposited on carbon- coated 400 mesh copper grid and evaporated under air. The images were analysed by Image J software and GMS 3 Analytical PC system.

CN crystallinity was determined using an Ultima IV X-ray diffractometer (XRD, Rigaku Co.,Japan) with Cu anode (Cu- Kα radiation = 0.15406 nm). The radiation source generator operated at an accelerating voltage of 40 kV and applied current of 44 mA. The analysis was performed with the PDXL2® software and the patterns were determined with the use of the XRD reference patterns reported in the Joint Committee on Powder Diffraction Standards (JCPDS) database.

The X-ray photoelectron spectroscopy (XPS) spectrum of CN was acquired with a XR50 Specs GmbH spectrometer using Mg K(α) as the excitation source and a PHOIBOS 100 half sphere electron energy analyser. A two-point calibration of the energy scale was performed using sputtered cleaned gold (Au 4f7/2, binding energy (BE) 84.00 eV) and copper (Cu 2p3/2, BE: 932.67 eV) samples. Internal calibration to correct for surface charging was done with the C 1 s peak at BE = 284.5 eV due to adventitious carbon. A Shirley-type background and a Gaussian-Lorentzian fitting and typical FWHM of 1.7 eV were used to analyse the chemical environment of the atoms from each high-resolution spectrum.

The infrared ATR spectrum of CN was acquired in an Agilent Cary Series 630 spectrometer equipped with ZnSe accessory. The solid sample was put in the holder and 64 scans in the range of 600–4000 cm^{-1} at a resolution of 4 cm^{-1} were recorded.

Diffuse transmittance spectra were recorded with a double-beam PGI-T90+ UV–vis spectrophotometer equipped with a $BaSO_4$ integrating sphere in a 0.1 cm quartz cuvette.

The surface area of the sample was measured using a Micromeritics equipment ASAP 2020 V1.02 E to obtain the nitrogen adsorption and desorption isotherms at 77 K. Before the measurement, the sample was dried overnight at 100 °C at a residual pressure of about 10^{-2} mbar to guarantee a good cleaning of the sample surface. Isotherm were analysed by means of BET model.

2.4. Photocatalytic measurements

Continuous UV irradiation experiments were performed in a Rayonet (Southern N.E. UltravioletCo.) reactor equipped with four 350 ± 20 nm lamps. The photon flux of the lamp was measured with the potassium ferrioxalate chemical actinometer [17]. The photon flux reaching the system was $I_0 = 1.47 \times 10^{-8}$ Ein. s^{-1} cm^{-3}. A volume of 3 mL of 20 mg/L aqueous suspensions of the photocatalyst sample and 1×10^{-5} M of methyl orange (MO) were placed in a 10 mm-path quartz cuvette and submitted to continuous magnetic stirring. Before illumination, the samples were maintained in the dark for 30 min. At different time intervals, the samples were taken and filtered with acetate 0.22 μm pore size membranes. The UV–vis absorption spectra of the filtrates were obtained, and the absorption at 465 nm were compared with initial values to calculate the discoloration as $MO\ removal\% = \left(1 - \frac{A(t)}{Ao}\right)x100$, where A(t) is the 465 nm absorbance at time t, A_0 is the initial absorbance at 465 nm. To study the influence of oxygen concentration and the formation of reactive species formed during irradiation, the suspensions were saturated with Ar, air or O_2, prior to irradiation. To investigate time-evolution of H_2O_2 concentration, continuous experiments were performed irradiating 100 mL of 20 mg/L aqueous suspensions of the photocatalyst sample and 1×10^{-5} M of methyl orange (MO) were placed in a quartz cylindrical tube and submitted to continuous magnetic stirring. At different time intervals, 3 mL of the samples were taken and filtered with acetate 0.22 μm pore size membranes and their absorbance measured as described above. In later case, the photon flux reaching the cuvette was $I_0 = 5.05 \times 10^{-9}$ Ein.s^{-1} cm^{-3}.

Aiming to investigate the reactive species ($O_2^{\bullet -}$, $HO^{\bullet}$, h^+, e^- and $^1O_2$) involved in MO photocatalytic degradation, specific scavengers were added during the photocatalytic test up to 180 min. Consequently, in separated assays 1.0 mM of ascorbic acid (AA) was incorporated as a $O_2^{\bullet -}$ quencher; 20 mM of isopropanol (IPA) was added as a quencher of $HO^{\bullet}$; 20 mM triethylamine (TEA) was included as a h^+ quencher; 1.0 mM sodium azide (SA) was put as a quencher of $^1O_2$ and finally 50 mM of MV^{2+} was added as hydrated electron (e^-_{aq}) scavenger. Additionally, superoxide radical and/or H_2O_2 formation were determined indirectly by an enzymatic colorimetric method employing a commercial kit for cholesterol quantification, Colestat Wiener Lab Argentina, measuring the H_2O_2 concentration. Calibration curves were done using standard

H_2O_2 commercial solutions. Also, photocatalytic experiments with the external addition of 100 μM of H_2O_2 were performed and compared with the MO/CN assay. Finally, irradiation of CN/MO/H_2O_2 in the absence and in the presence of 400 mg/L catalase, an enzyme that catalyses specifically the decomposition of H_2O_2 into H_2O and O_2 was also performed.

Hydroxyl radical formation during CN irradiation was tested by reaction with terephthalic acid scavenger yielding a luminescent product. To that purpose, a mass of 20 mg of CN were suspended in 100 mL of ultrapure water. Then, terephthalic acid were added (4 mM) and the final pH was adjusted to 8.7. The suspension was stirred in the dark for 30 min before illumination with 4 lamps of 350 nm. After different time intervals, 3 mL samples were withdrawn and immediately filtered through a 0.2 nm acetate cellulose membrane. The samples were then analysed by recording the photoluminescence spectra with a Jobin-Yvon Spex Fluorolog FL3–11 Spectrometer equipped with a Xe lamp as the excitation source, a monochromator with 1 nm bandpass gap for selecting the excitation and emission wavelengths, and a red sensitive R928 PM detector. The spectra were corrected for the wavelength-dependent sensitivity of the detector and the light source and the emission spectra were corrected for Raman scattering by using the solvent emission spectrum. The excitation wavelength was 320 nm and the emission maximum obtained was 425 nm for 2-hydroxy terephthalic acid (HTA). The excitation and the emission slits were both set to the width of 5 nm.

2.5. Electrochemical measurements

To determine the photoelectrochemical behaviour of the photoanodes based on the synthesized nanoparticles, working electrodes were prepared by deposition of CN nanoparticles under different conditions. Metrohm-DropSens (110) screen-printed carbon electrodes were used for deposition and CN nanoparticles were fixed by *dip-coating*. First, a suspension of 1.0 mg CN/mL of a 1:1 ethanol:water solution was prepared and submitted to ultrasonic bath for 30 min. After dropping the suspension on the electrodes, they were covered with a beaker and dried with a heating gun for 10 min (CN-A). To optimize the quantity of photoelectroactive material on the electrode, the previous process was repeated consecutively 3 times (CN-B).

The electrochemical signal was evaluated in 0.1 M Na_2SO_4 electrolyte solutions previously bubbled with N_2 for 15 min. The electrochemical measurements were performed under illumination of the electrode|electrolyte interface with a 3 W lamp centred at 395 ± 5 nm, ILULED. The reference electrode used was Ag-AgCl in all cases. Electrochemical measurements were done using a DropSens Potentiostat and photocurrent measurements were performed using linear sweep voltammetry (LSV) at 5 mV/s. [18,19]

Mott-Schottky plots for CN was carried out in the dark using differential capacitance (C) *vs.* potential (E) measurements [20]. The energy levels of the conduction (E_{CB}) and valence band (E_{VB}) for CN, were estimated considering the obtained E_g (found from diffusion reflectance absorption spectrum) and the corresponding E_{CB} value obtained from fit the experimental data (C *vs.* E) to the linear form of the Mott - Schottky equation (see Supporting Information). The value of E_{CB} is assumed to be equal to flat band potential, E_{FB} (obtained from above equation), and $E_{VB} = E_{CB} + E_g$ [21]. More details on E_{VB} and E_{CB} calculation are given in Supporting Information.

In order to verify that $HO^{\bullet}$ are formed by electrochemically assistance of the photocatalysis on CN, 50 μL of 8 ppm radical trap solution *N*, *N*-dimethyl-*p*-nitrosoaniline (RNO) was placed in the presence of the supporting electrolyte on the CN electrode and a CA experiment at 1.2 V *vs.* Ag-AgCl and illumination for 15 min have been performed. The chemical principle is based on the selective reaction between the specific reaction between $HO^{\bullet}$ and RNO, forming a stable adduct (RNO-OH), which reduces the 440 nm absorption band in the visible spectrum of RNO [22–24]. The UV–visible absorption spectra of the initial and the final solutions were measured with a Perkin Elmer Lambda 25 spectrophotometer, after a dilution to a final volume of 1 mL.

2.6. Stable product identification

For product detection, aqueous solutions of the MO (1×10^{-5}M) with and without the addition of 20 mg/L of CN were submitted to 180 min irradiation with four 350 nm lamps. After 0.22 μm filtration, the solutions were injected in an Alliance 2695 HPLC (Waters) coupled to a Quattro Premier XE (Waters) spectrometer. A CSH C18 (75 mm × 4,6 mm ID) Waters column was used. The eluent was a mixture of methanol–water gradient. MS detector used Ar as collision gas and an electrospray ionization source in positive mode at 100 °C and according to ionization conditions of each analyte; N_2 was used as drying and nebulizing gas at 400 °C and mass detection was performed in the range from 50 to 300 amu. The detection system was optimized by varying cone energy between 10 and 50 V and collision between 5 and 50 V.

2.7. Toxicity assay

Bioluminescent assays were carried out according to the standardised ISO 11348–3 norm, using lyophilised *V. fischeri* bacteria provided by Microtox. A standard procedure was employed for reconstitution of the bacteria. First, 1 mL of reconstitution solution at 4 °C was added to freeze-dried bacteria and transfer to a vial with 12 mL diluent (NaCl, 2%). The suspension was incubated for 20 min at 15 °C. Secondly, the pH of different samples: 1) 1×10^{-5} M of MO, 2) adsorption at 30 min of MO with CN and 3) photocatalytic degradation mixture after 15, 30, 60, 120, 180 min of irradiation was checked to be between 6.0 and 8.0. Third, the osmolarity of these samples was adjusted by adding 100 μL of saline solution (NaCl, 22%) and the mixtures were equilibrated for 5 min at 15 °C. Lastly, the inhibition of bioluminescence was determined in mixtures of 0.5 mL of bacterial suspension and 0.5 mL of samples. The decrease in bacterial luminescence (INH%) due to the presence of toxic chemicals is determined as: $\%\ INH = 100 - \left(\frac{IT_t}{IT_0 \times IB_t / IB_0}\right) \times 100$, where: IB_0 and IT_0 are the luminescence of blank and test samples at $t = 0$, respectively, and IB_t and IT_t are luminescence values for blank and test samples measured after $t = 15$ min and $t = 30$ min exposure, respectively. Ultrapure water was used as a reference sample.

3. Results and discussion

3.1. Characterization of CN photocatalyst

Fig. 1 presents the characterization results of CN. The XRD patterns presented in Fig. 1a showed a diffraction peak at $2\theta = 27.5°$, and a minor peak at 13.2°, assigned to the in-plane distance between two adjacent heptazine units (210 plane) [25] and the inter-layer sheet distance (stacking; 002 plane) [25], respectively. Adsorption-desorption isotherm at 77 K of N_2 gas on CN sample was obtained (Fig. S1). Modelling of the N_2 isotherm with BET model yields a surface area of 54.7 m^2/g and a pore volume of 0.19 cm^3/g with an average size of 13.7 nm, in line with an expected porous structure of g-C_3N_4 obtained upon NH_3, CO_2 and H_2O evolution during synthesis [26,27]. TEM micrographs show high agglomeration of the particles (Fig. 1b). HRTEM image of CN sample depicted in Fig. 1b show crystalline domains. The diffraction patterns in Fig. 1b correspond to plane distances of 0.32 nm in line with the XRD plane (002). IR-ATR spectrum of CN, see Fig. 2a, present typical peaks associated with CN heterocycles, as bands at 1530 and 1450 cm^{-1} and at 810 cm^{-1} correspond to 1,3,5-*s*-triazine ring stretching and breathing modes, respectively [28]. The peak at 1205 cm^{-1} is associated to C—N of primary amines [29]. The presence of a small broad peak beyond 3000 cm^{-1} is indicative of the N—H stretching in primary (3350–3180 cm^{-1}) and secondary (3320–3070 cm^{-1}) amides

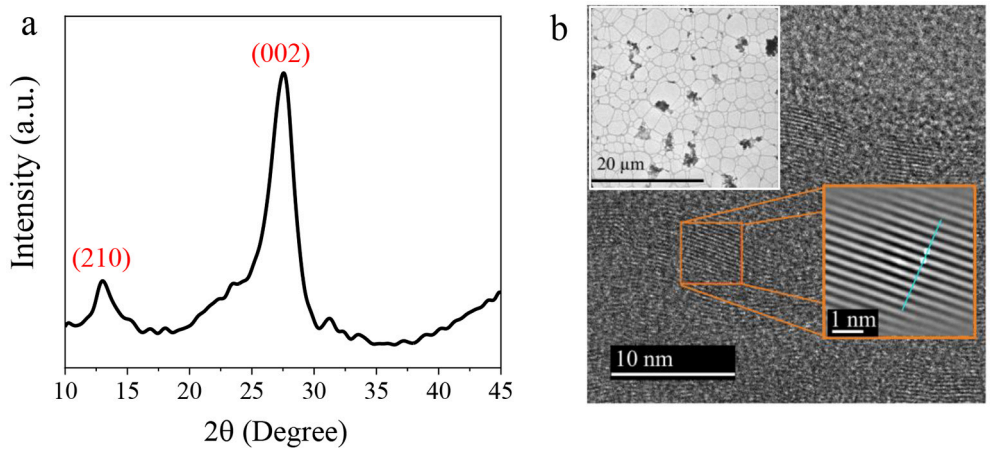

Fig. 1. (a) X-ray diffraction (XRD) pattern of CN, dotted lines stands for 210 and 002 planes angles (b) HRTEM image of CN particle *Inset:* TEM images of CN showing particle agglomeration.

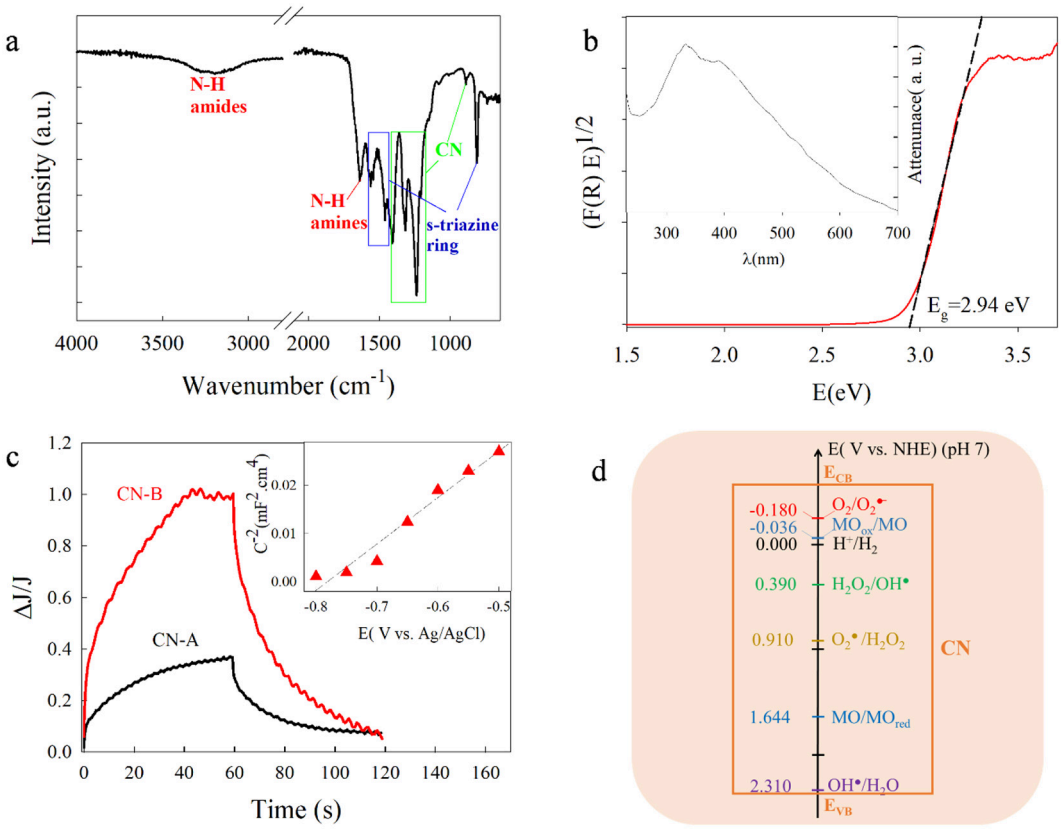

Fig. 2. (a)ATR-IR spectra of CN solid sample, (b) UV − vis/DRS spectra (*inset*) and Tauc plots of synthesized CN with n = ½. Absorption edge is marked with dashed line (c) Linear sweep voltammetry obtained for CN-A and CN-B electrodes. *Inset*: Mott–Schottky plot obtained with electrode CN-B. The potential is plotted against Ag/AgCl. The flat band potential is obtained from the intercept with potential axes and converted in E *vs.* NHE. (d) Redox potentials (E *vs.* NHE at pH 7) for couples involved in the reaction mechanism. Orange rectangle shows the valence and conduction band potential.

and their intermolecular hydrogen bonds [26].

XPS was further employed to investigate the surface chemical composition. The XPS survey spectrum of CN present the characteristic bands of C, N, and O, accounting for surface oxidized CN. Fig. S2 depict C 1 s, N 1 s, and O 1 s bands analysed. The ratios of the areas N:C and O:C XPS peaks (not considering the contribution of spurious C), each corrected by the atomic and instrument sensitivity factors, provide an average composition of $C_1N_{0.63}O_{1.42}$. The N:C ratio obtained deviates from the expected for the g-C_3N_4 structure, being an indication for a more defective structure and incomplete condensation. Formation of oxygen–enriched carbon nitride, during calcination in air atmosphere, was reported in literature from different precursors [11,30,31]. The incorporation of oxygen functionalities on the CN structure was reported be beneficial for the development of visible active photocatalysts. In that sense, Long et al. used urea as an only precursor and demonstrated by DFT calculation and experimental characterization that the introduction of oxygen improve the photocatalytic activity, by improving the separation efficiency of photogenerated carriers and inhibiting their

recombination [30]. Further, an improved efficiency and selectivity of photocatalytic oxygen reduction to produce H_2O_2 was obtained for oxygen-enriched carbon nitride polymers, which can more easily form 1,4-endoperoxide species rather than superoxide radicals [11].

Optical and photoelectrochemical measurements were performed to obtained complementary information for CN photocatalyst characterization. The UV–vis diffused reflectance spectrum of CN, see Fig. 2b, allows the estimation of the band gap energy (E_g) by the Tauc approach considering indirect transitions. [32] To that purpose, the equation: $[F(R\infty)E]^{1/2}$ *vs.* E was used, where $E = h\nu$. The intercept of the tangents in plots yielded a value of $E_g = 2.94$ eV, showing its potential visible light photoactivity.

Photoelectrochemical studies were performed using electrodes formed by the synthetized CN sample. Fig. 2c presents the LSV of the CN-A and CN-B electrodes prepared with different covering procedure, as described above. Both electrodes show a notable increment in current intensity with increasing potential until a steady state is reached. After light interruption, a decay of the current is evidenced which responds to a slow deactivation process. This behaviour may be due to the existence of surface states and deep traps. A higher photocurrent was observed for CN-B, which, after three cycles of illumination and darkness, show identical photocurrent characteristics as can be seen in Fig. S3 accounting for sample reproducibility and ability to be reused.

Photocurrent comes from the flow of electrons that is defined by electrochemically assisted photocatalysis, specifically from the oxidation of water that occurs at the electrode|electrolyte interface [33]. It should be noted that the photocurrent is observed at high overpotentials, indicating the need to polarize the interface to promote water oxidation. In that sense, a qualitative test to evaluate the presence of $HO^\bullet$ during the electrochemical assistance of photocatalysis on CN-B electrode was performed and a decrease (38%) in the absorption band at 440 nm of RNO solution after 15 min of CA experiment at 1.2 V was obtained, confirming the $HO^\bullet$ electrochemical generation (Fig. S4).

The Mott-Schottky plots (Fig. 2c *inset*) showed a linear region with a positive slope typical of the *n*-type material. A flat band potential (E_{FB}) of −0.60 v *vs.* NHE was obtained from the intercept of the linear portion of the Mott–Schottky plot with the potential axes, in coincidence with that reported for g-CN obtained by pyrolysis (−0.66 and − 0.76 V *vs.* NHE) [31]. Considering the latter value as the conduction band potential (E_{CB}) and taking $E_g = 2.94$ eV, as obtained from optical experiments, the valence band potential is $E_{VB} = 2.34$ V *vs.* NHE [21]. Obtained E_{CB} and E_{VB} strongly indicate that the obtained CN is able, both, to reduce (−0.036 V *vs.* NHE) and oxidize (1.644 V *vs.* NHE) [34] MO. Also, it is able to reduce molecular oxygen to $O_2^{\bullet-}$ ($E(O_2/O_2^{\bullet-}) = -0.18$ V) [35] and to oxidize water to hydroxyl radical (2.30 V *vs.* NHE at pH = 7) [23,36,37].

3.2. Photocatalytic experiments

Methyl Orange aqueous solutions 1×10^{-5} M were exposed to 350 nm irradiation in the presence and absence of 20 mg/L of CN after 30 min equilibration in the dark. The percentage of MO removal is displayed in Fig. 3. MO removal in the absence of CN is < than 7%, as expected from the low light absorption of the dye at 350 nm. The presence of CN increased drastically MO removal, which reached >94% of degradation in 210 min. The pH remained in the range 6–7 during experiments.

According to literature reports [38,39], among the reactive species, which may participate in the photocatalytic process, are superoxide radical anions ($O_2^{\bullet-}$), hydroxyl radicals ($HO^\bullet$), singlet oxygen ($^1O_2$) and migrated holes (h^+) and electrons (e^-). The unambiguous identification of these species is of importance for the understanding of the photocatalytic efficiency of CN nanoparticles. To that purpose, additional photocatalytic experiments were conducted upon 350 nm irradiation of 1×10^{-5} M MO aqueous solutions in the presence of CN and of specific reactive species scavengers. Tetraethylamine (TEA) [40] and methyl viologen (MV^{2+}) [41] were used as specific h^+ and e^- scavengers, respectively, while isopropyl alcohol (IPA) [42], ascorbic acid (AA) [43], and sodium azide (SA) [41] were used as scavengers of $HO^\bullet$ radicals, $O_2^{\bullet-}$ radical anions, and singlet oxygen ($^1O_2$). Since at long irradiation times, a complex reaction mixture evolves due to the formation of unidentified reaction products and secondary intermediates which could further complicate the understanding of the reactive species initiating MO degradation, mainly degradation rates up to 30 min will be considered, corresponding to *ca.* 30% MO degradation. The results obtained are depicted in Fig. 4.

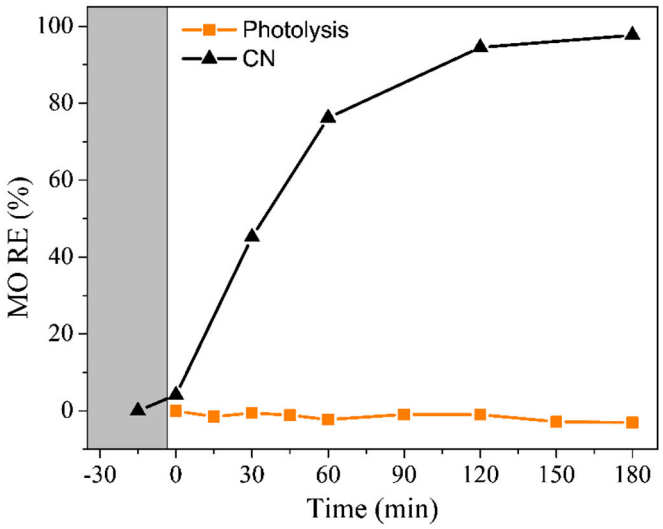

Fig. 3. MO removal *vs* irradiation time of an initial MO concentration $c_0 = 1 \times 10^{-5}$ M in the presence (black) and absence (orange) of 20 mg/L of CN upon 350 nm irradiation. Dark contact period is marked as grey zone.

To facilitate the understanding of the observed results, a simplified reaction mechanism is postulated, based on the known processes reported in the literature. Charge separation after light absorption (reaction (1)) is the initial process leading to photogenerated electron-hole pairs $CN(e^-, h^+)$.

$$CN + h\nu \rightarrow CN(e^-, h^+) \quad (1)$$

Several possibilities for MO reaction pathways with photogenerated charge carriers and secondary reactive species formed after them may be envisaged.

Reactions involving photogenerated holes (h^+): The reaction of h^+ with H_2O (reaction (2)) and MO (reaction (3)) are plausible reactions, as discussed earlier. Such reactions are expected to occur both, in the absence and presence of dissolved molecular oxygen. The occurrence of reaction (3) is in line with the fact that irradiation of oxygen - saturated CN in the presence of tetraethyl amine (TEA), a specific h^+ scavenger, showed a small inhibiting effect on MO discoloration rate (see Fig. 4c).

$$CN(e^-, h^+) + H_2O \rightarrow HO^\bullet + H^+ + CN(e^-) \quad (2)$$

$$CN(e^-, h^+) + MO \rightarrow MO_{oxidized} + CN(e^-) \quad (3)$$

Moreover, reaction of $HO^\bullet$ radicals formed after reaction (2) with MO, reaction (4), is a possible reaction path initiating MO degradation. In fact, hole and hydroxyl radical competition for MO degradation was reported to be important at TiO_2 photocatalysis with $[MO] < 1 \times 10^{-4}$ M [44].

$$HO^\bullet + MO \rightarrow MO_{oxidized} \quad (4)$$

Reactions involving photogenerated electrons (e^-): As also discussed earlier, photogenerated electrons are able to reduce O_2 to superoxide radicals yielding $O_2^{\bullet-}$ [45], reaction (5). The observation that increasing concentrations of dissolved O_2 accelerate MO degradation process (see

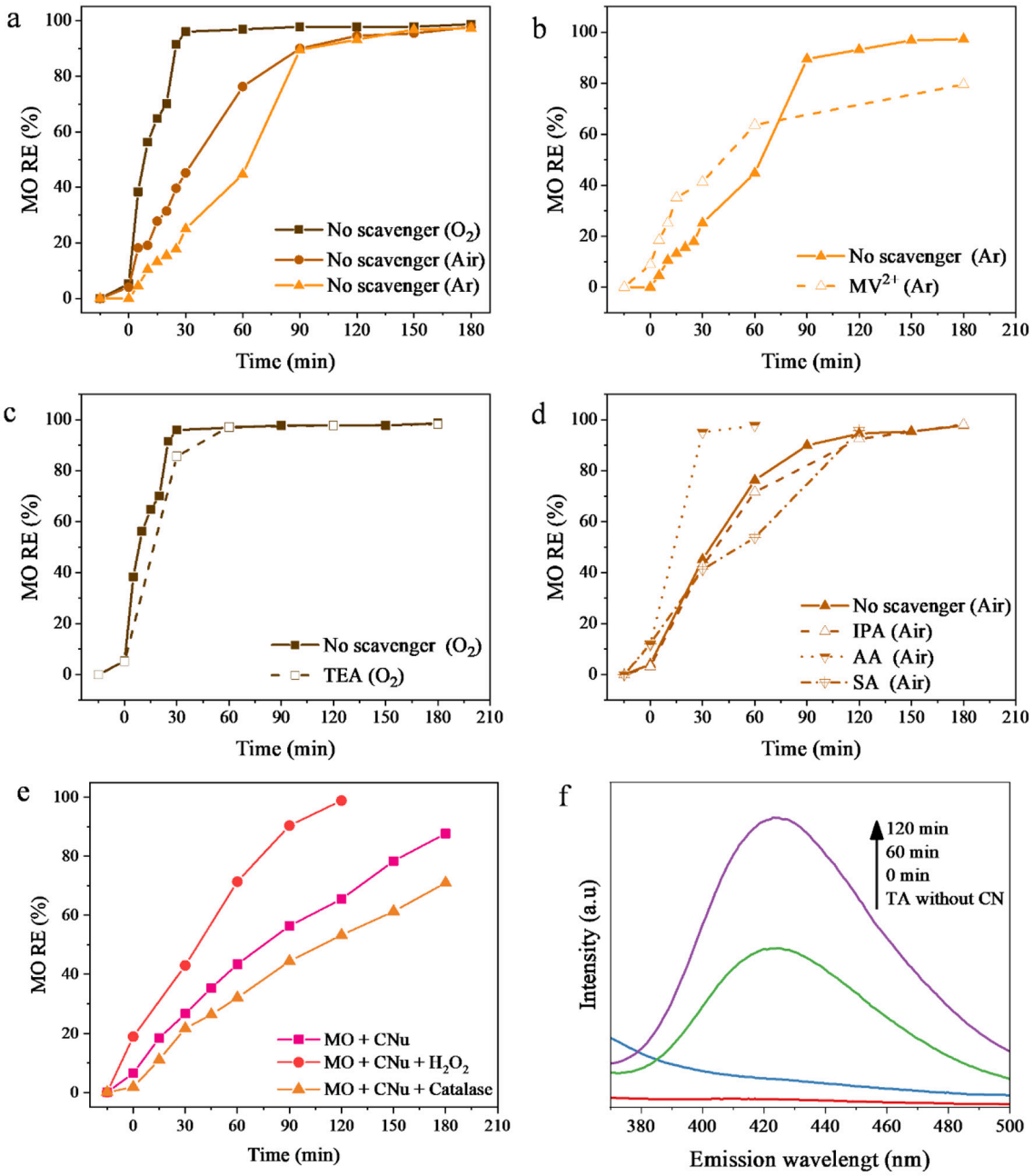

Fig. 4. Effect of the presence of (a) air, O_2, and Ar in the discoloration of MO in the presence of CN. Following figures refer to the addition of reactive species scavengers in the discoloration of MO in different saturated atmospheres: (b) argon-saturated suspensions in the presence (open symbols) and absence (black symbols) of MV^{2+}; (c) oxygen saturated suspensions in the presence (open symbols) and absence (black symbols) of TEA; (d) air-saturated suspensions in the absence (black circles) and presence of IPA (open circles), AA (black triangles), and SA (open triangles); (e) MO discoloration in the presence of additional H_2O_2 (open symbols) and additional H_2O_2 and catalase (black triangles); (f) Photoluminiscence spectra($\lambda_{exc} = 320$ nm) of the HTA aqueous solution resulting from the reaction of TA with $HO^{\bullet}$ radical generated by CN irradiation with 350 nm light.

Fig. 4a) strongly indicates that, O_2 scavenging of e^- may inhibit CN(e^- - h^+) pair recombination releasing more h^+ for reaction with MO. Since $O_2^{\bullet -}$ is a poor reductant, any reaction of MO with $O_2^{\bullet -}$ might be of little significance.

$$CN(e^-, h^+) + O_2 \rightarrow O_2^{\bullet -} + CN(h^+) \quad (5)$$

Since the photoreduction of MO mediated by photocatalysts is a reaction reported in the literature [46–49], the participation of the e^- in the discoloration of MO (reaction (6)) was tested in experiments performed in the presence of the e^- scavenger MV^{2+} in an Ar atmosphere to avoid $O_2^{\bullet -}$ participation. These experiments show that, initial MO degradation rate was accelerated in the presence of MV^{2+} in an argon atmosphere (see Fig. 4b), thus stressing the involvement of h^+ (or its reaction intermediates) in the removal of MO as a consequence of the inhibition of the (e^- - h^+) pair recombination by MV^{2+} (*vide supra*). Therefore, photoreduction, reaction (6) is of minor importance in our reaction system.

$$CN(e^-, h^+) + MO \rightarrow MO_{reduced} + CN(h^+) \quad (6)$$

The role of H_2O_2 in the overall reaction: Hydroxyl radical recombination, reaction (7) is a source of H_2O_2. However, superoxide radical anion formed from reaction (5) in experiments in the presence of O_2, may also

recombine to yield hydrogen peroxide, reaction (8). Interestingly, concentration of H_2O_2 in the absence and presence of MO under otherwise identical irradiation conditions were of ~1.4 and 17 μM, respectively, upon 180 min irradiation in a 3 mL cuvette ($I_0 = 1.47 \times 10^{-8}$ Eins.s^{-1}.cm^{-3}). MO aqueous solutions in the absence of CN yielded a production rate of ~2.3 μM H_2O_2, thus indicating that the dye on its own is not responsible for the observed increase. An increase in the concentration of hydrogen peroxide is observed with the irradiation time (Fig. S5). Therefore, the combined presence of CN and MO under irradiation leads to the formation of greater amounts of H_2O_2, in coincidence with reported values for 4-phenoxyphenol modified alkalinized CN framework [50] and surface oxygen-enriched CN [11], in accordance with our surface composition obtained from XPS. Hydroxyl radicals and $O_2^{\bullet-}$ radical anion recombination, reactions (7) and (8), and a two-step electron reduction of O_2, reactions (5) and (9), may be responsible for H_2O_2 formation in our experimental setup [9,50,51].

$$HO^{\bullet} + HO^{\bullet} \rightarrow H_2O_2 \quad (7)$$

$$O_2^{\bullet-} + O_2^{\bullet-} + 2H^+ \rightarrow H_2O_2 + O_2 \quad (8)$$

$$O_2^{\bullet-} + CN(e^-, h^+) + 2H^+ \rightarrow H_2O_2 + CN(h^+) \quad (9)$$

To elucidate the contribution of H_2O_2 to MO discoloration, an additional photocatalytic experiment was assessed. To that purpose, photocatalysis experiments were performed in air-saturated aqueous suspensions of CN and MO in the presence of an initial amount of added H_2O_2. The observed acceleration of MO discoloration rate strongly suggests the participation of H_2O_2, see Figure 4d, *inset*. Furthermore, addition of catalase, an enzyme capable of decomposing H_2O_2 to O_2 and H_2O, diminish MO discoloration rate, see Fig. 4e, emphasizing the H_2O_2 participation on MO degradation. The catalytic metal-free activation of H_2O_2 over graphitic carbon nitride in the dark and under visible light irradiation for Rhodamine B removal was reported previously [52]. Activation of H_2O_2 is considered as an environmentally-friendly oxidation, with H_2O as the side product [53]. In fact, reaction of H_2O_2 with hydrated electrons is reported to be very efficient [45], therefore, further reduction of H_2O_2 by photogenerated electrons, reaction (10), is an important reaction leading to $HO^{\bullet}$ radicals formation. Thus, reaction (10) is a further source of $HO^{\bullet}$ radicals available for initiating MO degradation through reaction (4). The latter reaction path seems to enhance MO discoloration with respect to MO reduction by e^- (reaction (6)).

$$H_2O_2 + CN(e^-, h^+) \rightarrow HO^{\bullet} + HO^- + CN(h^+) \quad (10)$$

Based on redox potentials, oxidation of H_2O_2 to $O_2^{\bullet-}$ by photogenerated holes, reaction (11), is a plausible reaction ($E_{red} = 0.95$ V at pH 7) [35]. Competition of MO and H_2O_2 for photogenerated holes (reactions (11) and (3)) would explain the increased H_2O_2 concentration observed mainly in the presence of MO.

$$CN(h^+) + H_2O_2 \rightarrow O_2^{\bullet-} + 2H^+ \quad (11)$$

Experiments carried out in air saturated suspensions of CN in the presence of ascorbic acid (AA), an $O_2^{\bullet-}$ scavenger, showed an acceleration of MO discoloration, see Fig. 4d. Similar results were also evidenced by Pan [54] in g-C_3N_4/MoS_2 composite photodegradation of MO and suggested that, since $O_2^{\bullet-}$ efficiently reacts with e^- to yield H_2O_2, reaction (5), its scavenging by AA increases the amount of e^- available for initiating MO discoloration. However, our scavenging experiments (*vide supra*) with MV^{2+} strongly suggested that MO reduction by electrons is not an important reaction.

Altogether, the fact that H_2O_2 addition enhances MO degradation rate, but quenching of $O_2^{\bullet-}$, a H_2O_2 precursor, also accelerates MO discoloration rate, strongly indicates that H_2O_2 is involved in a complex reaction pathway regulating the concentration of reactive species initiating MO degradation. In fact, $O_2^{\bullet-}$ and H_2O_2 compete for photogenerated electrons, reactions (9) and (10); therefore, diminution of $O_2^{\bullet-}$ concentration accelerates $HO^{\bullet}$ formation, and subsequently MO degradation by reaction (4).

The participation of $HO^{\bullet}$ radicals was investigated upon addition of its specific scavenger isopropyl alcohol (IPA) to the reaction mixture containing MO and the photocatalyst CN in an air-saturated atmosphere. Results show a slight diminution in the discoloration rate of MO, see Fig. 4d. However, addition of IPA as a $HO^{\bullet}$ radical scavenger is not the best choice, since α-hydroxyalkyl radicals formed from the reaction of IPA and $HO^{\bullet}$ are able to reduce O_2 to $O_2^{\bullet-}$ [35,55], thus activating the mechanism forming $HO^{\bullet}$ radicals previously discussed. Therefore, the obtained results may be taken as evidence supporting the participation of $HO^{\bullet}$ radicals in the MO degradation mechanism, reaction (4).

The generation of $HO^{\bullet}$ radicals by irradiation of CN was confirmed by the terephthalic acid (TA) assay. TA is a well-known $HO^{\bullet}$ specific scavenger which does not react with either H_2O_2, $O_2^{\bullet-}$ or $^1O_2$ [56]. The reaction product, 2-hydroxy terephthalic acid (HTA) present emission at 425 nm when excited with light of 320 nm. Fig. 4f shows the increased emission spectra of CN samples in the presence of TA with increasing irradiation times, thus strongly suggesting $HO^{\bullet}$ radical formation.

Furthermore, experiments in the presence of sodium azide (SA), a singlet oxygen ($^1O_2$) scavenger, resulted in a diminution of MO discoloration rate at the longer irradiation times, thus indicating the participation of $^1O_2$ in the reaction mechanism, reaction (12). In fact, $O_2^{\bullet-}$ could be a precursor for the generation of $^1O_2$ by reaction with photogenerated holes ($O_2^{\bullet-} + CN(h^+) \geq {}^1O_2$). However, when $O_2^{\bullet-}$ was scavenged by AA, MO discoloration increased suggesting that $O_2^{\bullet-}$ did not mediate the $^1O_2$ formation [3]. An energy transfer from excited triplet excitons to molecular oxygen is then suggested reaction (13). The energy transfer mechanism was demonstrated in carbonyl modified [57] g-C_3N_4 obtained through a simple chemical oxidation treatment of pristine g-C_3N_4 and in benzophenone modified carbon nitride [58].

$$^1O_2 + MO \rightarrow MO_{oxidized} \quad (12)$$

$$CN + h\nu \rightarrow CN^* \ (+ O_2) \rightarrow CN + {}^1O_2 \quad (13)$$

Based on the previous discussion, the scheme of reactions depicted in Scheme 1 represents a possible pathway for the primary steps of the CN photocatalytic degradation. The observation that CN is able to produce H_2O_2 in appreciable amounts, only in the presence of MO, is in line with reported studies of CN semiconductors combined with polyethyleneimine [9]. Functional Density theoretical studies on the latter systems demonstrated that the electronic interaction between polyethyleneimine and graphitic CN was able to promote the separation of the photogenerated charge carriers and the reduction of O_2 to H_2O_2 in two steps of one electron each. However, H_2O_2 generation by CN is still controversial. Some authors report that CN structures are able to degrade methylene blue [12] and paraquat [13], only if H_2O_2 is added in the reaction system. Other authors report the efficient formation of H_2O_2 upon irradiation of CN suspensions in the presence of ethanol as electron donors [10]. In the latter study, H_2O_2 was proposed to be formed through a two-electron reduction of 1,4-endoperoxides intermediates on the graphitic CN structure, thus avoiding formation of $O_2^{\bullet-}$ as an intermediate. The involvement of 1,4-endoperoxides in O_2 reduction to H_2O_2 was also proposed by other authors investigating the photocatalysis of O-enriched CN polymers [11], in line with our surface composition obtained by XPS. No simple correlation between the chemical nature, surface charge and reduction potential of the molecules and their ability (or inability) to induce H_2O_2 generation can be obtained. From an analysis of the reaction mechanism in Scheme 1, it may be expected that molecules inducing H_2O_2 generation should be capable of being adsorbed on CN surface and able to capture h^+ to improve electron-hole separation and allow O_2 to be reduced by two consecutive one-electron reactions. Weather formation of 1,4 endoperoxides on CN structure is a possible reaction pathway will be matter of a further study.

Primary and secondary reactive species formed after light-absorption

$$CN + h\nu \rightarrow CN(e^-, h^+) \quad (1)$$

$$CN(e^-, h^+) + H_2O \rightarrow HO^\bullet + H^+ + CN(e^-) \quad (2)$$

$$CN(e^-, h^+) + O_2 \rightarrow O_2^{\bullet-} + CN(h^+) \quad (5)$$

$$CN + h\nu \rightarrow CN^* (+O_2) \rightarrow CN + {}^1O_2 \quad (13)$$

Reactions leading to MO degradation

$$CN(e^-, h^+) + MO \rightarrow MO_{oxidized} + CN(e^-) \quad (3)$$

$$HO^\bullet + MO \rightarrow MO_{oxidized} \quad (4)$$

$$CN(e^-, h^+) + MO \rightarrow MO_{reduced} + CN(h^+) \quad (6)$$

$${}^1O_2 + MO \rightarrow MO_{oxidized} \quad (12)$$

Reactions leading to H_2O_2 generation

$$HO^\bullet + HO^\bullet \rightarrow H_2O_2 \quad (7)$$

$$O_2^{\bullet-} + O_2^{\bullet-} + 2H^+ \rightarrow H_2O_2 + O_2 \quad (8)$$

$$O_2^{\bullet-} + CN(e^-, h^+) + 2H^+ \rightarrow H_2O_2 + CN(h^+) \quad (9)$$

Reactions leading to H_2O_2 depletion

$$H_2O_2 + CN(e^-, h^+) \rightarrow HO^\bullet + HO^- + CN(h^+) \quad (10)$$

$$CN(h^+) + H_2O_2 \rightarrow O_2^{\bullet-} + 2H^+ \quad (11)$$

Scheme 1. Set of most probable reactions taking place upon visible irradiation of CN in the presence of MO. The numbering of the reactions follow the order in their description in the text. Herein, they are ordered differently to make easier the understanding of the reaction mechanism. Reaction (6) is shown for discussion purposes, though it was found to be of little importance.

3.3. Stable products identification

To further support these first conclusions stressing the ability of $^1O_2$, $CN(h^+)$, and $HO^\bullet$ of initiating MO discoloration, and the capacity of e^- and h^+ of regulating the amounts of H_2O_2, stable reaction intermediate products formed after the discoloration of MO were analysed.

Stable primary degradation products of aqueous solutions of 1×10^{-5}M of MO and MO solutions in the presence of 20 mg/L of CN upon 180 min photocatalysis were identified by liquid chromatography/MS assays. Table 1 summarizes the mass spectrometry (MS) peaks observed for the degradation products of MO and product assignment. It is worth mentioning that the products detected are the result of long-term treatment, so they will be products with an advanced degree of degradation.

Table 1
m/z, retention time (Rt) and product assignment for aqueous solution of MO and MO/CN.

Sample	m/z; Rt	Product assignment
MO	306(b.p M + H),328(M + Na); Rt = 4.84 min	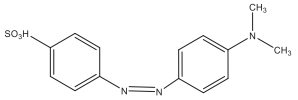
MO + CN	Reaction Product 1 288 (M + H), 274 (b.p.), 230,157; Rt = 5.15 min	P1 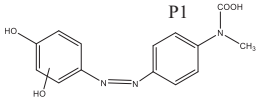
	Reaction Product 2 338 (M + Na), 316(M + H), 279 (b.p.), 181; Rt = 5.57 min	P2 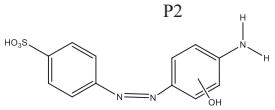

After irradiation, two main chromatographic peaks were observed at retention times (Rt) of 5.15 and 5.57 min, respectively, different from that of MO. The MS spectra of MO present two peaks having m/z = 306 and 328 which is assigned to [MO + H] and [MO + Na].

The MS spectra of the chromatographic peak with Rt = 5.15 min (denoted as product P1) presents a MS peak m/z = 288 assigned to [P1 + H]. The presence of ruptures in the ionization chamber leading to m/z 274, 230 and 157 may be explained by characteristic ruptures of reaction product P1. On the other hand, the chromatographic peak with R_t = 5.57 min (corresponding to reaction product P2) present MS peaks at m/z 338 (P2 + Na) and 316 (P2 + H) and ruptures at m/z 279 (base peak) and 181 which may be explained by the proposed structure P2.

Formation of products P1 and P2 involves the successive attack of either $HO^\bullet$, $CN(h^+)$, or $^1O_2$ on different parts of the molecule. Both, P1 and P2 show an $HO^\bullet$ radical attack on MO benzyl rings involving a charge transfer and water addition leading to the hydroxylation of benzyl, see reaction (A) in Scheme 2. P1 also shows $HO^\bullet$ radical addition to the C bearing the sulfonate group; further elimination of sulfonate also leads a hydroxylated benzyl, see reaction (B) in Scheme 2. Attack of either $HO^\bullet$, $CN(h^+)$, or $^1O_2$ on dimethylamine nitrogen involves a charge transfer and further elimination of a H^+ from the methyl α carbon, which upon O_2 addition leads to peroxide radical formation. Recombination of the latter radicals and O_2 elimination leads to -N-COH groups, which releases H_2CO_2 yielding amine [59], as also shown in reaction (C) in Scheme 2.

Therefore, P1 involves two $HO^\bullet$ radical attacks on the benzyl ring, one of which took place in position *ipso* to the sulfonate group, and an $^1O_2$ or $CN(h^+)$ charge transfer reaction on the amide N, reactions A, B, and C, respectively. Formation of P2 involves one $HO^\bullet$ radical attack on the benzyl ring and an $^1O_2$ or $CN(h^+)$ charge transfer reaction on the amide N, reactions A, and C, respectively. Consequently, the nature of the observed products formed after MO photocatalytic treatment may be explained by well-known characteristic reactions of $CN(h^+)$ [60], $HO^\bullet$ radicals [16,61,62] and $^1O_2$ excited state [62], as expected from reactions (3), (4), and (12) respectively in Scheme 1.

The reaction of photogenerated e^- to promote MO reduction was largely reported in literature [46–49,63,64]. MO reduction may occur *via* two-electron transfer to the dye to yield the hydrazine derivative of MO (see S.I. Scheme S1). Further $2e^-$ reduction of hydrazine may produce amine derivatives as $C_8H_{12}N_2$ and $C_6H_7NO_3S$ [65]. Since such reaction products were not detected in our air saturated reaction system, we further conclude that MO reduction by photogenerated electrons is not an important reaction taking place in air saturated suspensions probably because of the preferential electron transfer to O_2 molecules.

3.4. Toxicity of MO and its photocatalytic degradation products

The INH% of 1×10^{-5}M MO solutions before and after different irradiation times (t = 15, 30, 60, 120, 180 min) in the presence and absence of CN, were evaluated after 15 and 30 min incubation times. Since results after 15 and 30 min incubation are similar, only data for 30 min incubation are shown in Fig. 5. The INH% of MO solutions, both in the absence and presence of CN, reaches >95%, stressing an important toxicity of the initial compounds to the bacteria. In that sense, non-negligible toxicity were reported by Song *et al*, [66] which observed a 45% inhibition for a [MO] = 1.5×10^{-4} M. Moreover, other authors reported a 50% inhibition with a [MO] 5×10^{-5} M [67]. After 15 min of irradiation in the presence of CN, the luminescence inhibition remains at high values. The toxicological assays reveal that partial discoloration of the dye (*ca.* 20%) after 15 min of irradiation does not necessary relate with its detoxification, as was previously reported for other textile dyes [68]. After 30 min of illumination, a decrease to 60% of inhibition was observed. That implies that reaction mixtures after short-term irradiation may have less toxicity that initial MO molecule. However, upon

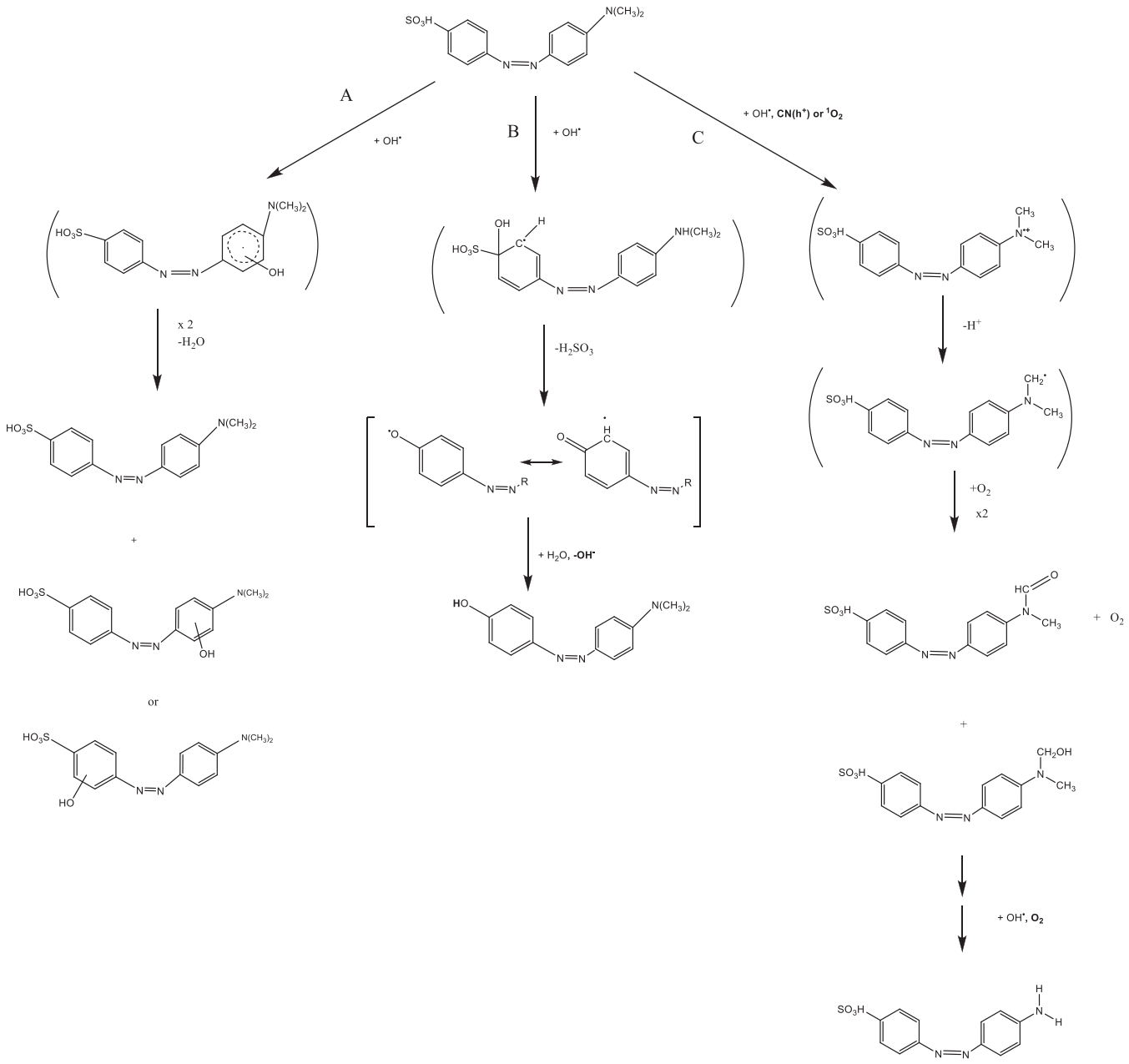

Scheme 2. Reaction paths leading to the oxidation of MO upon visible light irradiation of air saturated CN suspensions containing MO.

continuous irradiation, an increase in %INH was observed, which could be ascribed to the generation of by-products causing greater toxicity [66]. Only after 180 min of irradiation, an important decrease of toxicity was observed (INH% = 22%). Formation of products P1 and P2 took place after 180 min irradiation. Therefore, it could be concluded that stable metabolites observed in Scheme 2, have a reduced toxicity against *Vibrio fischeri* compared to the parent MO.

4. Conclusions

To summarize, carbon nitride nanosheets synthetized from urea present crystalline domains coincident with that of heptazine units (known as "melon") and porous structure with a BET surface area > 50 m^2/g probably related to gases evolution during thermal condensation. Photoelectrochemical and optical studies allowed to determine a band gap energy $E_g = 2.94$ eV, and conduction and valence band potentials $E_{CB} = -0.60$ V and $E_{VB} = 2.34$ V *vs* NHE strongly indicating that the obtained CN is able to reduce O_2 to $O_2^{\bullet -}$ and to oxidize H_2O to $HO^\bullet$ radicals.

Methyl orange CN-mediated photocatalytic degradation upon 350 nm irradiation show good photocatalytic performance in air saturation conditions. Additional quenching experiments and the determination of the nature of the reaction products demonstrated the participation of h^+, $^1O_2$, and $HO^\bullet$ in MO degradation. A reaction mechanism was proposed based on the obtained photocatalytic and electrochemical results and the stable product detection by LC- MS. The complex reaction mechanism involved competitive reactions among primary and secondary species photogenerated after CN irradiation. MO terminal amino groups and the benzene rings are the most labile fragments of the molecule against these oxidizing species.

$HO^\bullet$ radicals were obtained by the direct oxidation of water (reaction 2) but also generated *via* the successive three-electron reduction of molecular oxygen O_2 (+ e^-) → $O_2^{\bullet -}$ (+ e^-) → H_2O_2 (+ e^-) → $HO^\bullet$, reactions (5), (9) and (10), respectively. The latter sequence of reactions

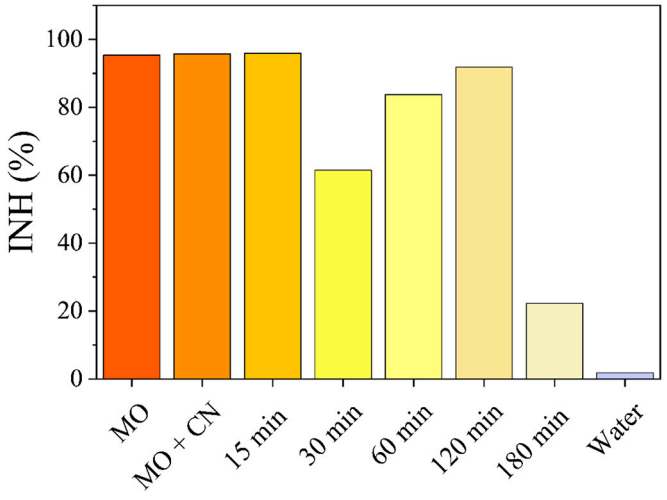

Fig. 5. *Vibrio fischeri* bioluminiscense inhibition for aqueous solution of MO, aqueous solution of MO after 30 min contact with CN (MO + CN), and after different irradiation times in the presence of CN (15, 30, 60, 120, 180 min). Ultrapure water is also displayed as a reference.

was observed to be an important path contributing to MO depletion. It is interesting to note that, despite oxidative reactive radicals h^+, $^1O_2$, and $HO^\bullet$ are responsible for MO degradation, an important path for the production of hydroxyl radicals involves a reductive reaction pathway. Remarkably, CN enables the use of both photogenerated charge carriers (e^- and h^+) in MO oxidative degradation.

Formation of H_2O_2 in the reductive pathway of O_2 is an important aspect of the photocatalyst. However, the presence of an organic molecule capable of interacting with photogenerated holes, such as MO, is of fundamental importance to enhance its formation. Otherwise, H_2O_2 is converted back to $O_2^{\bullet-}$ upon reaction with CN(h^+), reaction (11). Reactions (9) and (11) constitute an endless loop, needing the scavenging of CN(h^+), to make profit of the generation of $HO^\bullet$ radicals by reaction (10). In coincidence with literature reports [9], the MO interaction with CN enhance CN(e^- - h^+) pair separation, allowing the electrons to reduce O_2 to H_2O_2 and the further reduction of the latter to $HO^\bullet$ radicals. Despite the advances herein presented concerning the reaction mechanisms involved and the role of H_2O_2 in CN photocatalytic degradation of MO, it is still important to determine which CN structures and surface compositions are able to promote H_2O_2 generation.

Herein, we disentangle the MO photocatalytic degradation mechanism initiated by multiple reactive primary and secondary species obtained from CN irradiation. However, we demonstrated that discoloration of methyl orange under such oxidative conditions might not improve the water quality, as the primary products of degradation still show toxicity to *Vibrio fischeri*. However, reduced toxicity might be obtained with an advanced degree of MO oxidation involving HO– addition to benzene ring, HO– substitution of sulfonic acid group and oxidation of α-C amine metabolites.

CRediT authorship contribution statement

Laura S. Gómez Velázquez: Investigation, Formal analysis, Validation. **María L. Dell'Arciprete:** Investigation, Writing – original draft, Writing – review & editing, Supervision, Conceptualization. **Lorean Madriz:** Investigation, Validation, Methodology, Writing – original draft. **Mónica C. Gonzalez:** Funding acquisition, Writing – review & editing, Conceptualization.

Declaration of Competing Interest

The authors declare the following financial interests/personal relationships which may be considered as potential competing interests:

Monica C. Gonzalez reports financial support was provided by Agencia Nacional de Promoción Científica y Tecnológica.

Data availability

No data was used for the research described in the article.

Acknowledgements

This research was supported by Consejo Nacional de Investigaciones Científicas y Técnicas (CONICET). L.S.G.V. and L.M. thanks CONICET for their graduate and postdoctoral studentship respectively. M.L.D. and M.C.G. are research members of CONICET. The authors also want to acknowledge the financial support of Agencia Nacional de Promoción Científica y Tecnológica (PICT 2019-01509).

Appendix A. Supplementary data

Supplementary data to this article can be found online at https://doi.org/10.1016/j.catcom.2023.106617.

References

[1] J. Lin, W. Tian, H. Zhang, X. Duan, H. Sun, H. Wang, Y. Fang, Y. Huang, S. Wang, Carbon nitride-based Z-scheme heterojunctions for solar-driven advanced oxidation processes, J. Hazard. Mater. 434 (2022), 128866, https://doi.org/10.1016/j.jhazmat.2022.128866.

[2] X. Wang, K. Maeda, A. Thomas, K. Takanabe, G. Xin, J.M. Carlsson, K. Domen, M. Antonietti, A metal-free polymeric photocatalyst for hydrogen production from water under visible light, Nat. Mater. 8 (2009) 76–80, https://doi.org/10.1038/nmat2317.

[3] Y. Chen, B. Wang, W. Hou, Graphitic carbon nitride embedded with graphene materials towards photocatalysis of bisphenol A: the role of graphene and mediation of superoxide and singlet oxygen, Chemosphere. 278 (2021), 130334, https://doi.org/10.1016/j.chemosphere.2021.130334.

[4] A. Torres-Pinto, M.J. Sampaio, C.G. Silva, J.L. Faria, A.M.T. Silva, Recent strategies for hydrogen peroxide production by metal-free carbon nitride photocatalysts, Catalysts. 9 (2019), https://doi.org/10.3390/catal9120990.

[5] T. Zhang, W. Schilling, S.U. Khan, H.Y.V. Ching, C. Lu, J. Chen, A. Jaworski, G. Barcaro, S. Monti, K. De Wael, A. Slabon, S. Das, Atomic-level understanding for the enhanced generation of hydrogen peroxide by the introduction of an aryl amino group in polymeric carbon nitrides, ACS Catal. 11 (2021) 14087–14101, https://doi.org/10.1021/acscatal.1c03733.

[6] J. Chen, N. Kang, J. Fan, C. Lu, K. Lv, Carbon nitride for photocatalytic water splitting to produce hydrogen and hydrogen peroxide, Mater. Today Chem. 26 (2022), 101028, https://doi.org/10.1016/j.mtchem.2022.101028.

[7] M. Li, Q. Zheng, D.P. Durkin, H. Chen, D. Shuai, Environmental application of chlorine-doped graphitic carbon nitride: continuous solar-driven photocatalytic production of hydrogen peroxide, J. Hazard. Mater. 436 (2022), 129251, https://doi.org/10.1016/j.jhazmat.2022.129251.

[8] Y. Kofuji, Y. Isobe, Y. Shiraishi, H. Sakamoto, S. Ichikawa, S. Tanaka, T. Hirai, Hydrogen peroxide production on a carbon nitride–boron nitride-reduced graphene oxide hybrid photocatalyst under visible light, ChemCatChem. 10 (2018) 2070–2077, https://doi.org/10.1002/cctc.201701683.

[9] X. Zeng, Y. Liu, Y. Kang, Q. Li, Y. Xia, Y. Zhu, H. Hou, M.H. Uddin, T. R. Gengenbach, D. Xia, C. Sun, D.T. Mccarthy, A. Deletic, J. Yu, X. Zhang, Simultaneously tuning charge separation and oxygen reduction pathway on graphitic carbon nitride by polyethylenimine for boosted photocatalytic hydrogen peroxide production, ACS Catal. 10 (2020) 3697–3706, https://doi.org/10.1021/acscatal.9b05247.

[10] Y. Shiraishi, S. Kanazawa, Y. Sugano, D. Tsukamoto, H. Sakamoto, S. Ichikawa, T. Hirai, Highly selective production of hydrogen peroxide on graphitic carbon nitride (g-C 3 N 4) photocatalyst activated by visible light, ACS Catal. 4 (2014) 774–780, https://doi.org/10.1021/cs401208c.

[11] Z. Wei, M. Liu, Z. Zhang, W. Yao, H. Tan, Y. Zhu, Efficient visible-light-driven selective oxygen reduction to hydrogen peroxide by oxygen-enriched graphitic carbon nitride polymers, Energy Environ. Sci. 11 (2018) 2581–2589, https://doi.org/10.1039/C8EE01316K.

[12] D. Saha, M.M. Desipio, T.J. Hoinkis, E.J. Smeltz, R. Thorpe, D.K. Hensley, S. G. Fischer-Drowos, J. Chen, Influence of hydrogen peroxide in enhancing photocatalytic activity of carbon nitride under visible light: an insight into reaction intermediates, J. Environ. Chem. Eng. 6 (2018) 4927–4936, https://doi.org/10.1016/j.jece.2018.07.030.

[13] M.M. Desipio, R. Thorpe, D. Saha, Photocatalytic decomposition of paraquat under visible light by carbon nitride and hydrogen peroxide, Optik (Stuttg) 172 (2018) 1047–1056, https://doi.org/10.1016/j.ijleo.2018.07.124.

[14] B. Lellis, C.Z. Fávaro-Polonio, J.A. Pamphile, J.C. Polonio, Effects of textile dyes on health and the environment and bioremediation potential of living organisms,

Biotechnol. Res. Innov. 3 (2019) 275–290, https://doi.org/10.1016/j.biori.2019.09.001.
[15] R. Krishnamoorthy, A.R. Choudhury, P.A. Jose, K. Suganya, M. Senthilkumar, J. Prabhakaran, N.O. Gopal, J. Choi, K. Kim, R. Anandham, T. Sa, Long-term exposure to azo dyes from textile wastewater causes the abundance of saccharibacteria population, Appl. Sci. 11 (2021) 1–8, https://doi.org/10.3390/app11010379.
[16] M.L. Dell'Arciprete, L. Santos-Juanes, A. Arques Sanz, R. Vicente, A.M. Amat, J. P. Furlong, D.O. Martire, M.C. Gonzalez, A.A. Sanz, R. Vicente, A.M. Amat, J. P. Furlong, D.O. Mártire, M.C. Gonzalez, Reactivity of hydroxyl radicals with neonicotinoid insecticides: mechanism and changes in toxicity, Photochem. Photobiol. Sci. 8 (2009) 1016–1023, https://doi.org/10.1039/b900960d.
[17] H.J. Kuhn, S.E. Braslavsky, R. Schmidt, Chemical actinometry, Pure Appl. Chem. 76 (2004) 2105–2146, https://doi.org/10.1351/pac198961020187.
[18] L. Madriz, J. Tatá, D. Carvajal, O. Núñez, B.R. Scharifker, J. Mostany, C. Borrás, F. M. Cabrerizo, R. Vargas, Photocatalysis and photoelectrochemical glucose oxidation on Bi_2WO_6: conditions for the concomitant H_2 production, Renew. Energy 152 (2020) 974–983, https://doi.org/10.1016/j.renene.2020.01.071.
[19] R. Vargas, L. Madriz, V. Márquez, D. Torres, Z.C. Kadirova, K. Yubuta, M. Hojamberdiev, Elucidating the enhanced photoelectrochemical performance of zinc-blende ZnS/wurtzite ZnO heterojunction and adsorption of water molecules by molecular dynamics simulations, Mater. Sci. Semicond. Process. 142 (2022), 106494, https://doi.org/10.1016/j.mssp.2022.106494.
[20] A. Hankin, F.E. Bedoya-lora, J.C. Alexander, Flat Band Potential Determination: Avoiding the Pitfalls †, Journal of Materials Chemistry A (2019) 26162–26176, https://doi.org/10.1039/c9ta09569a.
[21] P.J. Espinoza-Montero, R. Vargas, P. Alulema-Pullupaxi, L. Fernández, Photoelectrocatalysis: Principles and applications, in: G.Y.T. Maulin, P. Shah, Sweta Parimita Bera (Eds.), Adv. Oxid. Process. Wastewater Treat, 1st ed, CRC Press, Boca Raton, Florida, 2022, p. 298.
[22] C. Comninellis, Electrocatalysis in the electrochemical conversion/combustion of organic pollutants for waste water treatment, Electrochim. Acta 39 (1994) 1857–1862.
[23] Y. Nosaka, A.Y. Nosaka, Generation and detection of reactive oxygen species in photocatalysis, Chem. Rev. 117 (2017) 11302–11336, https://doi.org/10.1021/acs.chemrev.7b00161.
[24] L. Madriz, M. Parra, F.S. García Einschlag, O. Núñez, F.M. Cabrerizo, R. Vargas, Photocatalytic oxidation of urea on surface-modified Bi_2WO_6 with trans-4-stilbenecarboxaldehyde, J. Phys. Chem. C 125 (2021) 12682–12689, https://doi.org/10.1021/acs.jpcc.1c03063.
[25] F. Fina, S.K. Callear, G.M. Carins, J.T.S. Irvine, Structural investigation of graphitic carbon nitride via XRD and neutron diffraction, Chem. Mater. 27 (2015) 2612–2618, https://doi.org/10.1021/acs.chemmater.5b00411.
[26] Y. Zheng, Z. Zhang, C. Li, A comparison of graphitic carbon nitrides synthesized from different precursors through pyrolysis, J. Photochem. Photobiol. A Chem. 332 (2017) 32–44, https://doi.org/10.1016/j.jphotochem.2016.08.005.
[27] P. Yang, J. Zhao, W. Qiao, L. Li, Z. Zhu, Ammonia-induced robust photocatalytic hydrogen evolution of graphitic carbon nitride, Nanoscale. 7 (2015) 18887–18890, https://doi.org/10.1039/c5nr05570a.
[28] N.D. Shcherban, P. Mäki-Arvela, A. Aho, S.A. Sergiienko, P.S. Yaremov, K. Eränen, D.Y. Murzin, Melamine-derived graphitic carbon nitride as a new effective metal-free catalyst for Knoevenagel condensation of benzaldehyde with ethylcyanoacetate, Catal. Sci. Technol. 8 (2018) 2928–2937, https://doi.org/10.1039/C8CY00253C.
[29] X. Yuan, K. Luo, K. Zhang, J. He, Y. Zhao, D. Yu, Combinatorial vibration-mode assignment for the FTIR spectrum of crystalline melamine: a strategic approach toward theoretical IR vibrational calculations of triazine-based compounds, J. Phys. Chem. A 120 (2016) 7427–7433, https://doi.org/10.1021/acs.jpca.6b06015.
[30] X. Long, C. Feng, S. Yang, D. Ding, J. Feng, M. Liu, Y. Chen, J. Tan, X. Peng, J. Shi, R. Chen, Oxygen doped graphitic carbon nitride with regulatable local electron density and band structure for improved photocatalytic degradation of bisphenol A, Chem. Eng. J. 435 (2022), 134835, https://doi.org/10.1016/j.cej.2022.134835.
[31] M. Ismael, Y. Wu, D.H. Taffa, P. Bottke, M. Wark, Graphitic carbon nitride synthesized by simple pyrolysis: role of precursor in photocatalytic hydrogen production, New J. Chem. 43 (2019) 6909–6920, https://doi.org/10.1039/c9nj00859d.
[32] P. Makuła, M. Pacia, W. Macyk, How to correctly determine the band gap energy of modified semiconductor photocatalysts based on UV-vis spectra, J. Phys. Chem. Lett. 9 (2018) 6814–6817, https://doi.org/10.1021/acs.jpclett.8b02892.
[33] Laurence M. Peter, Photoelectrochemistry: From basic principles to photocatalysis, in: Photocatal. Fundam. Perspect, Royal Society of Chemistry, 2016, pp. 1–28, https://doi.org/10.1039/9781782622338-00001.
[34] L.V. Trandafilovic, D.J. Jovanovic, X. Zhang, S. Ptasinska, M.D. Dramicanin, Enhanced photocatalytic degradation of methylene blue and methyl orange by ZnO: Eu nanoparticles, Appl. Catal. B Environ. 203 (2017) 740–752, https://doi.org/10.1016/j.apcatb.2016.10.063.
[35] P. Wardman, Reduction potentials of one-electron couples involving free radicals in aqueous solution, J. Phys. Chem. Ref. Data 18 (1989) 1637–1755, https://doi.org/10.1063/1.555843.
[36] S. Cheeseman, A.J. Christofferson, R. Kariuki, D. Cozzolino, T. Daeneke, R. J. Crawford, V.K. Truong, J. Chapman, A. Elbourne, Antimicrobial metal nanomaterials: from passive to stimuli-activated applications, Adv. Sci. 7 (2020), https://doi.org/10.1002/advs.201902913.
[37] W.H. Koppenol, D.M. Stanbury, P.L. Bounds, Electrode potentials of partially reduced oxygen species, from dioxygen to water, Free Radic. Biol. Med. 49 (2010) 317–322, https://doi.org/10.1016/j.freeradbiomed.2010.04.011.
[38] Y. Yang, X. Li, C. Zhou, W. Xiong, G. Zeng, D. Huang, C. Zhang, W. Wang, B. Song, X. Tang, X. Li, H. Guo, Recent advances in application of graphitic carbon nitride-based catalysts for degrading organic contaminants in water through advanced oxidation processes beyond photocatalysis: a critical review, Water Res. 184 (2020), 116200, https://doi.org/10.1016/j.watres.2020.116200.
[39] X. Kong, X. Liu, Y. Zheng, P.K. Chu, Y. Zhang, S. Wu, Graphitic carbon nitride-based materials for photocatalytic antibacterial application, Mater. Sci. Eng. R. Rep. 145 (2021), 100610, https://doi.org/10.1016/j.mser.2021.100610.
[40] W. Peng, Y. Lin, Z. Wan, H. Ji, W. Ma, J. Zhao, An unusual dependency on the hole-scavengers in photocatalytic reductions mediated by a titanium-based metal-organic framework, Catal. Today 340 (2020) 86–91, https://doi.org/10.1016/j.cattod.2018.11.038.
[41] M.J. Llansola Portolés, P.M.D. Gara, M.L. Kotler, S. Bertolotti, E.S. Román, H. B. Rodríguez, M.C.M.C. Gonzalez, Silicon nanoparticle photophysics and singlet oxygen generation, Langmuir. 26 (2010) 10953–10960, https://doi.org/10.1021/la100980x.
[42] M. Yoon, Y. Oh, S. Hong, J.S. Lee, R. Boppella, S.H. Kim, F. Marques Mota, S. O. Kim, D.H. Kim, Synergistically enhanced photocatalytic activity of graphitic carbon nitride and WO3 nanohybrids mediated by photo-Fenton reaction and H2O2, Appl. Catal. B Environ. 206 (2017) 263–270, https://doi.org/10.1016/j.apcatb.2017.01.038.
[43] J. Huang, J. Liu, L. Tian, X. Li, X. Ma, X. Yu, Q. Guo, J. Zhao, Ultrathin carbon-coated Zr3+-ZrO2 nanostructures for efficient visible light photocatalytic antibiotic elimination, Chem. Eng. J. 412 (2021), 128621, https://doi.org/10.1016/j.cej.2021.128621.
[44] L. Yu, J. Xi, M. De Li, H.T. Chan, T. Su, D.L. Phillips, W.K. Chan, The degradation mechanism of methyl orange under photo-catalysis of TiO 2, Phys. Chem. Chem. Phys. 14 (2012) 3589–3595, https://doi.org/10.1039/c2cp23226j.
[45] G.V. Buxton, C.L. Greenstock, W.P. Helman, A.B. Ross, Critical review of rate constants for reactions of hydrated electrons, hydrogen atoms and hydroxyl radicals (*OH/*O[sup -] in aqueous solution), J. Phys. Chem. Ref. Data 17 (1988) 513–886, https://doi.org/10.1063/1.555805.
[46] G.T. Brown, J.R. Darwen, Photoreduction of methyl orange sensitized by colloidal titanium dioxide, J. Chem. Soc. Faraday Trans. 80 (1984) 1631–1643.
[47] J. Peral, A. Mills, Factors affecting the kinetics of methyl orange reduction photosensitized by colloidal CdS, J. Photochem. Photobiol. A Chem. 73 (1993) 47–52.
[48] R. Chatti, S.S. Rayalu, N. Dubey, N. Labhsetwar, S. Devotta, Solar-based photoreduction of methyl orange using zeolite supported photocatalytic materials, Sol. Energy Mater. Sol. Cells 91 (2007) 180–190, https://doi.org/10.1016/j.solmat.2006.08.009.
[49] S. Oros-Ruiz, R. Gómez, R. López, A. Hernández-Gordillo, J.A. Pedraza-Avella, E. Moctezuma, E. Pérez, Photocatalytic reduction of methyl orange on Au / TiO2 semiconductors, Catal. Commun. 21 (2012) 72–76, https://doi.org/10.1016/j.catcom.2012.01.028.
[50] Y. Hu, P. Zhang, J. Du, C. Kim, S. Han, W. Choi, Bifunctional carbon nitride exhibiting both enhanced photoactivity and residual catalytic activity in the post-irradiation dark period, ACS Catal. 11 (2021) 14941–14955, https://doi.org/10.1021/acscatal.1c04564.
[51] L. Chen, C. Chen, Z. Yang, S. Li, C. Chu, B. Chen, Simultaneously tuning band structure and oxygen reduction pathway toward high-efficient photocatalytic hydrogen peroxide production using cyano-rich graphitic carbon nitride, Adv. Funct. Mater. 31 (2021) 1–10, https://doi.org/10.1002/adfm.202105731.
[52] Y. Cui, Z. Ding, P. Liu, M. Antonietti, X. Fu, X. Wang, Metal-free activation of H2O2 by g-C 3N4 under visible light irradiation for the degradation of organic pollutants, Phys. Chem. Chem. Phys. 14 (2012) 1455–1462, https://doi.org/10.1039/c1cp22820j.
[53] M. Antonietti, N. Lopez-Salas, A. Primo, Adjusting the structure and electronic properties of carbons for metal-free carbocatalysis of organic transformations, Adv. Mater. 31 (2019) 1–15, https://doi.org/10.1002/adma.201805719.
[54] Y. Pan, M. Yin, H. Fang, L. Xu, H. Yan, Enhanced photocatalytic performance of protonated graphite carbon nitride / molybdenum sulphide heterojunction for degradation of methyl orange dye, Mater. Technol. 00 (2020) 1–12, https://doi.org/10.1080/10667857.2020.1794293.
[55] T. Lund, D.D.M. Wayner, M. Jonsson, A.G. Larsen, K. Daasbjerg, Oxidation potentials of α-hydroxyalkyl radicals in acetonitrile obtained by photomodulated voltammetry, J. Am. Chem. Soc. 123 (2001) 12590–12595, https://doi.org/10.1021/ja011217b.
[56] J. Liu, T. An, Z. Chen, Z. Wang, H. Zhou, T. Fan, D. Zhang, M. Antonietti, Carbon nitride nanosheets as visible light photocatalytic initiators and crosslinkers for hydrogels with thermoresponsive turbidity, J. Mater. Chem. A 5 (2017) 8933–8938, https://doi.org/10.1039/c7ta02923c.
[57] H. Wang, S. Jiang, S. Chen, D. Li, X. Zhang, W. Shao, Enhanced singlet oxygen generation in oxidized graphitic carbon nitride for organic, Synthesis (2016) 1–6, https://doi.org/10.1002/adma.201601413.
[58] W. Wu, C. Han, Q. Zhang, Q. Zhang, Z. Li, D.J. Gosztola, G.P. Wiederrecht, M. Wu, Functionalizing carbon nitride with heavy atom-free spin converters for enhanced 1 O 2 generation, J. Catal. 361 (2018) 222–229, https://doi.org/10.1016/j.jcat.2018.03.006.
[59] M.L. Dell'Arciprete, C.J. Cobos, D.O. Mártire, J.P. Furlong, M.C. Gonzalez, Reaction kinetics and mechanisms of neonicotinoid pesticides with sulfate radicals, New J. Chem. 35 (2011), https://doi.org/10.1039/c0nj00726a.

[60] L. Jiang, X. Yuan, G. Zeng, X. Chen, Z. Wu, J. Liang, J. Zhang, H. Wang, H. Wang, Phosphorus- and sulfur-codoped g-C 3 N 4 : facile preparation, mechanism insight, and application as efficient photocatalyst for tetracycline and methyl orange degradation under visible light irradiation, ACS Sustain. Chem. Eng. 5 (2017) 5831–5841, https://doi.org/10.1021/acssuschemeng.7b00559.
[61] M.G. Gonzalez, E. Oliveros, M. Wörner, A.M. Braun, Vacuum-ultraviolet photolysis of aqueous reaction systems, J. Photochem. Photobiol. C Photochem. Rev. 5 (2004) 225–246, https://doi.org/10.1016/j.jphotochemrev.2004.10.002.
[62] M.L. Dell'Arciprete, L. Santos-Juanes, A. Arques, R.F. Vercher, A.M. Amat, J. P. Furlong, D.O. Mártire, M.C. Gonzalez, Reactivity of neonicotinoid pesticides with singlet oxygen, Catal. Today 151 (2010) 137–142, https://doi.org/10.1016/j.cattod.2010.01.020.
[63] A. Mills, A. Grenn, Methyl orange as a probe of photoelectrochemical reactions sensitized by colloidal CdS, J.Photochem. Photobiol.A: Chem. 59 (1991) 199–208.
[64] M.M. Joshi, N.K. Labhsetwar, P.A. Mangrulkar, S.N. Tijare, S.P. Kamble, S. S. Rayalu, Visible light induced photoreduction of methyl orange by N-doped mesoporous titania, Appl. Catal. A Gen. 357 (2009) 26–33, https://doi.org/10.1016/j.apcata.2008.12.030.
[65] H.H. Mohamed, N.A. Alomair, Exploiting stored TiO 2 electrons for multi-electron reduction of an azo dye methyl orange in aqueous suspension, J. Saudi Chem. Soc. 22 (2018) 322–328, https://doi.org/10.1016/j.jscs.2016.06.002.
[66] W. Song, J. Li, X. Zhang, J. Feng, X. Du, Q. Wang, C. Fu, W. Qiu, Z. Wang, X. Gao, A feasible approach for azo-dye methyl orange degradation in siderite / H_2O_2 assisted by persulfate: optimization using response surface methodology and pathway, J. Environ. Manag. 308 (2022), https://doi.org/10.1016/j.jenvman.2021.114397.
[67] R. Moya, M. Hernández, A.B. García-martín, A.S. Ball, M.E. Arias, Bioresource technology contributions to a better comprehension of redox-mediated decolouration and detoxification of azo dyes by a laccase produced by Streptomyces cyaneus CECT 3335, Bioresour. Technol. 101 (2010) 2224–2229, https://doi.org/10.1016/j.biortech.2009.11.061.
[68] J. Duarte Baumer, A. Valério, S.M.A.G.U. de Souza, G.S. Erzinger, A. Furigo, A.A. U. de Souza, Toxicity of enzymatically decolored textile dyes solution by horseradish peroxidase, J. Hazard. Mater. 360 (2018) 82–88, https://doi.org/10.1016/j.jhazmat.2018.07.102.